

Ultrafast **Single-Layer** Carbonization of Molybdenum Carbide Nanoparticles for Efficient Hydrogen Generation

Zhipeng Huang,^{*[a]} Cuncai Lv,^[a] Qianpeng Yang,^[a] Guangfeng Wei,^[a] Caofeng Pan,^{*[b]}
Zuofeng Chen,^[a] Mark G Humphrey,^[a,c] and Chi Zhang^{*[a]}

[a] School of Chemical Science and Engineering, Tongji University, Shanghai, 200092,
P. R. China

[b] Beijing Institute of Nanoenergy and Nanosystems, Chinese Academy of Sciences,
Beijing, 100083, P. R. China

[c] Research School of Chemistry, Australian National University, Canberra, ACT 2601,
Australia

Corresponding author: Zhipeng Huang, zphuang@tongji.edu.cn,

Chi Zhang, chizhang@tongji.edu.cn

Caofeng Pan, cfpan@binn.cas.cn

Abstract. A facile and ultrafast synthesis of molybdenum carbide coated with a single layer of carbon (MoC/C) has been developed, and the effect of reducing the thickness of carbon coating on hydrogen evolution reaction (HER) catalytic activity has been demonstrated. MoC/C produces a current density of 20 mA cm^{-2} at an overpotential of 144 mV and a Tafel slope of 63.6 mV dec^{-1} in 0.5 M H_2SO_4 , and is thereby one of the most active carbide electrocatalysts reported thus far, although MoC is not even the most active phase of molybdenum carbide and MoC/C has a small surface area. MoC/C performs under long-term electrolysis with little degradation. Complementary density functional theory calculations have afforded insight into this novel catalyst design, showing that increasing the thickness of the graphene layer results in the composite system losing the characteristics of MoC and behaving more like a graphene surface, and thereby resulting in a reduction in HER activity.

Keywords: molybdenum carbide • hydrogen evolution reaction • carbon coating • ultrasonic spray pyrolysis

INTRODUCTION

The increasing interest in hydrogen as an energy source has been triggered by severe environmental pollution, global warming and the depletion of fossil fuels. The splitting of water to hydrogen via the hydrogen evolution reaction (HER) is one of the most promising solutions to achieve a clean and renewable energy source.¹ Broad-ranging applications of water splitting require active, economical, and stable electrocatalysts for the HER. Although noble metals, e.g. platinum, demonstrate excellent activity in the HER, their high cost and scarcity hinder industrial applications. The development of efficient, low-cost, and stable non-precious metal electrocatalysts is therefore of great significance and urgently needed.

Amongst candidate HER electrocatalysts (e.g. metal chalcogenides,²⁻⁵ phosphides,⁶⁻¹⁰ and borides,¹¹ and metal-free nanocarbons¹²⁻¹³), **molybdenum carbide** and **tungsten carbide** have gained special attention because of their unique Pt-like d-band electronic structures.^{11, 14-32} **Great efforts have been devoted to promote the catalytic activity of these carbides by controlling their particle size,^{19-21, 26} phase,^{17, 27} and extent of carbide doping,^{18, 24} as well as doping of nanocarbon support.^{19, 25}** However, their **promise has not thus far been fully realized due to the** excessive surface carbon coatings that are normally formed during carbonization. Although it is intuitively known that a **thick** surface carbon coating is harmful, the extent to which it influences the activity of carbides remains unclear, and the mitigation of surface coke remains a major challenge. The difficulty arises from the excess carbon-containing precursors that are employed to avoid sintering of **molybdenum carbide and tungsten carbide** during high temperature (>700 °C) carbonization,^{11, 14-32} or from the fast and uncontrollable deposition of carbon during carbonization using gaseous carbon precursors.³³⁻³⁴ Leshkov et al. reported that carbonization of tungsten oxide buried in a SiO₂ matrix generated metal-terminated tungsten carbide, but the yield via this method is relatively low.³⁴ Li et al. reported that coke deposition on the surface of tungsten carbide can be mitigated by using carbon

nanotubes as a solid carbon source, but the carbonization has to be carried out under vacuum with a precisely controlled pressure.²⁹ Chen et al. reduced the surface carbon coating on WC by an oxygen plasma, but the method is only applicable to planar surfaces and a plasma generator is required.³⁵ Because **molybdenum carbide** offers promise not only in the field of HER,^{11, 14-32} but also in various electrocatalysis applications, e.g. oxygen reduction,³⁶ methanol oxidation,³⁷ and triiodide reduction,³⁸⁻³⁹ **a high-yielding synthesis of mono/few-layer carbon-coated molybdenum carbides is highly desirable and will undoubtedly accelerate the development of these novel materials.**

Herein molybdenum carbide nanoparticles coated with a single carbon layer (MoC/C) were synthesized by a convenient and scalable ultrasonic spray pyrolysis (USP) method, and shown to be relatively active and stable for the HER in acidic solution. **With an overpotential of 144 mV required to drive the current density of 20 mA cm⁻², MoC/C is proved to be one of the most active carbide electrocatalysts reported thus far. Correlation of the performance of MoC to the thickness of its carbon coating has been demonstrated experimentally and rationalized theoretically. USP is a process that allows for continuous, easy, and large-scale production of nanoparticles, but previous syntheses using USP have overwhelmingly been dominated by oxides and chalcogenides.⁴⁰ We demonstrate for the first time that USP can be employed in the synthesis of metal carbides, and that the carbonization can be accomplished in an unexpectedly short time (<15 s). The results reported here offer a promising approach to the large-scale synthesis of highly efficient HER electrocatalysts, and a powerful way to promote catalytic activity of carbides.**

EXPERIMENTAL SECTION

Reagents

Molybdenum chloride (MoCl₅, AR), ethanol (LR), and silicon dioxide nanoparticles (SiO₂, ca. 15 nm diameter) were purchased from Aladdin Reagent (Shanghai) Co. Ltd.

All the chemicals were used following receipt without any further purification.

Synthesis of MoC/C

The MoC/C was synthesized by USP using the setup shown in Figure 1a. In a typical procedure, the precursor solution was prepared by dissolving MoCl₅ (1.00 g) in ethanol (100 mL). Prior to the USP, the quartz tube (850 °C) and the chamber of the nebulizer were flushed with nitrogen (99.99%) for 30 min to eliminate oxygen. Nitrogen (2 L min⁻¹) was used as the carrier gas to carry a mist containing the ethanol solution from the nebulizer chamber into the quartz tube. The product was collected on a woven wire mesh (stainless steel, 400 mesh) located at the cool zone in the down-stream direction of the quartz tube. After the reaction, the product was collected from the woven wire mesh.

Synthesis of MoC@C

The synthesis of MoC@C was similar to that of MoC/C except that SiO₂ nanoparticles (1.00 g) were added to the precursor solution and the precursor solution was sonicated for 30 min prior to the USP. After the reaction, the SiO₂ nanoparticles were removed by etching the collected powder in 10% HF for 24 h. The resultant MoC@C was then dried in vacuum at 80 °C for 24 h.

Characterization

The morphology, microstructure, and composition of samples were characterized by transmission electron microscopy (TEM, 300 kV, Tecnai G2 F30 S-TWIN, FEI), scanning electron microscopy (SEM, S-4800, Hitachi), X-ray diffraction (XRD, Bruker D8 Advance, Cu K α radiation, $\lambda = 1.54178 \text{ \AA}$), Raman spectroscopy (ThermoFisher, $\lambda = 532 \text{ nm}$), and X-ray photoelectron spectroscopy (XPS, ESCALAB250Xi, ThermoFisher). Thermal gravimetric analysis (TGA) was performed with a STA449C thermal analyzer (NETZSCH) under an oxygen atmosphere at a heating rate of 10 °C min⁻¹. N₂-sorption

isotherms were collected on a NOVA 2000e instrument. Brunauer-Emmett-Teller (BET) specific surface areas were calculated from adsorption data.

Electrochemical measurements

All electrochemical measurements were carried out on a CHI 614D electrochemistry workstation with a three-electrode system. A graphite rod was used as the counter electrode, a mercury/mercurous sulfate electrode (MSE) or mercury/mercuric oxide electrode (MOE) was used as the reference electrode, and a glassy carbon electrode (GCE) loaded with the catalyst ink was used as the working electrode. For this purpose, the catalyst (4 mg), ethanol (1 mL) and Nafion solution (5 wt%, 80 μ L) were mixed by ultrasonication (130 W, 2 mm probe) for 1 h. Ten micro-liters of the resultant ink was pipetted onto the GCE and dried at room temperature (loading amount: 0.57 mg cm⁻²).

H₂ (99.999%) purged 0.5 M H₂SO₄ or 1 M KOH solution was used as the electrolyte. The reversible hydrogen evolution potential (RHE) was determined by measuring the open circuit potential of a clean Pt electrode in the solution of interest bubbled with H₂; the potential was -0.705 V versus MSE for the 0.5 M H₂SO₄ and -0.930 V versus MOE for the 1 M KOH solution. The scan rate was 5 mV s⁻¹ for the linear sweep voltammetry (LSV) measurements and 50 mV s⁻¹ for the cyclic voltammetry (CV) measurements. The uncompensated cell resistance (R) was determined via the current-interrupt method, and iR correction was performed with $\eta_{\text{corr}} = \eta - iR$. Electrochemical impedance spectroscopy (EIS) was performed at -0.2 V vs RHE from 10⁶ to 10⁻² Hz. The volume of H₂ during the potentiostatic electrolysis experiment was monitored by the water displacement method.

RESULTS AND DISCUSSION

As mentioned above, it is difficult to control the thickness of the surface carbon layer. Our strategy to overcome this problem involves controlling the reaction time while ensuring that all particles are subjected to equivalent heating, thereby affording a homogeneous product. This strategy was realized by a simple one-step USP of a mixture

of MoCl_5 and ethanol. During the USP, the precursor particles passed through the heating zone in series to ensure identical heating. Figure 1a shows the experimental setup. In brief, a mist of precursor droplets generated by a nebulizer was driven by nitrogen flow (2 L min^{-1}) through a quartz tube (4 cm inner diameter and 40 cm length) held at $850 \text{ }^\circ\text{C}$. MoC/C resulted from the pyrolysis of the precursors at the high temperature zone and was collected at the end of the quartz tube. The time for the materials to pass through the quartz tube was 15 s.

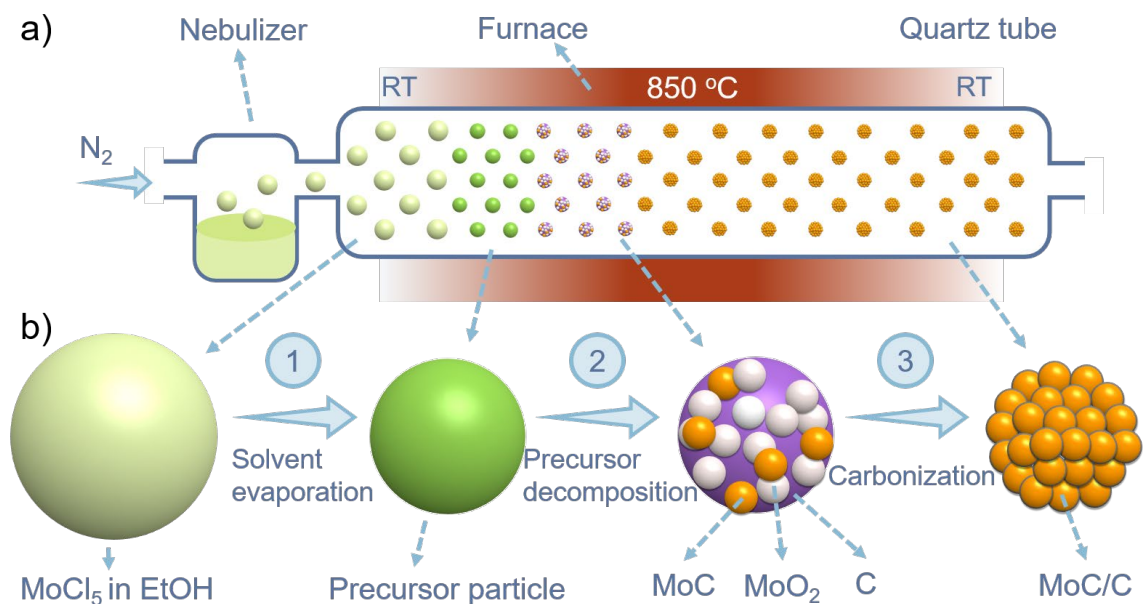


Figure 1. Illustration of (a) the synthesis setup and (b) the formation of MoC/C. RT: room temperature.

The process by which MoC/C is formed was investigated by a series of USP experiments carried out at different temperatures; the composition and structure of the corresponding products were analogous to intermediates generated at zones of the quartz tube during the growth of the MoC/C (Section 1, SI). The various intermediate products

were identified from XPS spectra and XRD patterns (Figure S1 to Figure S4, SI). The ethanolysis of MoCl_5 affords $\text{MoO}_{2.5-(2x+1)/2}(\text{OC}_2\text{H}_5)_x\text{Cl}_{x+1}$ ($x = 1, 2$).⁴¹⁻⁴² When droplets of precursor solution passed through the quartz tube, the fast evaporation of ethanol in the low temperature zone resulted in the precipitation of precursor particles containing Mo, C, O, and Cl, as illustrated by step 1 in Figure 1b. The decomposition of these precursor particles at higher temperature (e.g., 550 °C) gave composite particles of MoO_2 , carbon, and a small amount of MoC (step 2 in Figure 1b). The MoO_2 in the composites was further carbonized to give MoC (step 3 in Figure 1b). The carbon required for the carbothermal reduction is presumably derived from the precursor (i.e., $\text{MoO}_{2.5-(2x+1)/2}(\text{OC}_2\text{H}_5)_x\text{Cl}_{x+1}$) and/or the ethanol. To ascertain the origin of the carbon, an ethanol solution of phosphomolybdic acid was subjected to USP at 850 °C. In this case, only trace amounts of MoC were detected by XPS, while XRD showed no peaks from MoC (Figure S3, SI). Ethanol therefore cannot be responsible for most of the conversion of MoO_2 to MoC under these conditions, the carbonization of MoO_2 to MoC in MoC/C being primarily associated with the carbon from $\text{Mo}(\text{OC}_2\text{H}_5)_2\text{Cl}_3$. The pyrolysis of ethanol occurred in tandem with the formation of MoC, resulting in a carbon coating on the surface of the MoC particles. The short reaction time (< 15 s) is essential for avoiding a thick carbon coating on the surface of the MoC nanoparticles.

The complete carbonization of intermediate MoO_2 in 15 s is correlated with the homogeneous distribution of molybdenum in the single-source precursor. The single-source precursor ($\text{MoO}_{2.5-(2x+1)/2}(\text{OC}_2\text{H}_5)_x\text{Cl}_{x+1}$) is pyrolyzed to a composite in which the MoO_2 content is dispersed homogeneously in the carbon matrix, so that complete carbonization of MoO_2 is possible. We have also carried out a USP of an aqueous solution of ammonium molybdate, glucose, and sodium chloride at 850 °C.⁴³ Because ammonium molybdate and glucose have different solubilities, the resulting inhomogeneous precipitation of ammonium molybdate and glucose during USP produced an intermediate composed of large molybdenum oxide particles (> 100 nm) and carbon.

Lengthy (2 h) annealing was then required to convert this intermediate to Mo₂C, due to the large size of the molybdenum oxide particles and consequently their insufficient contact with carbon.

MoC@C was synthesized for comparison by an approach similar to that of MoC/C, except that SiO₂ nanoparticles (~ 15 nm diameter) were added to the growth solution as structural templates and were removed after the USP. Control experiments of the USP of phosphomolybdic acid in ethanol with and without SiO₂ nanoparticles showed that a much thicker carbon coating on the nanoparticles was found in samples synthesized with SiO₂ nanoparticles, in comparison with that without SiO₂ nanoparticles (Section 2 and Figure S3, SI), indicating that the pyrolysis of ethanol was promoted by SiO₂ nanoparticles. The catalytic pyrolysis of ethanol on the surface of the SiO₂ nanoparticles can be attributed to the surface defect sites correlated with the sphere morphology,⁴⁴ and the oxygen-bearing surface enhancing the absorption of hydrocarbons at high temperatures.⁴⁵ The promoted pyrolysis of ethanol resulted in a thick carbon coating on the surface of the MoC particles in the MoC@C.

Morphological features of MoC/C and MoC@C were revealed by electron microscopy. MoC/C consists of solid spheres with rough surfaces and ca. 500 nm diameter (Figures 2a and 2b). In contrast, the morphology of MoC@C is less regular (Figure 2c), and cavities can be seen on the MoC@C particles (Figure 2d). TEM confirmed that the MoC/C consists of solid spherical particles assembled by nanoparticles (Figure 2e), whereas copious pores exist in the MoC@C particles (Figure 2g).

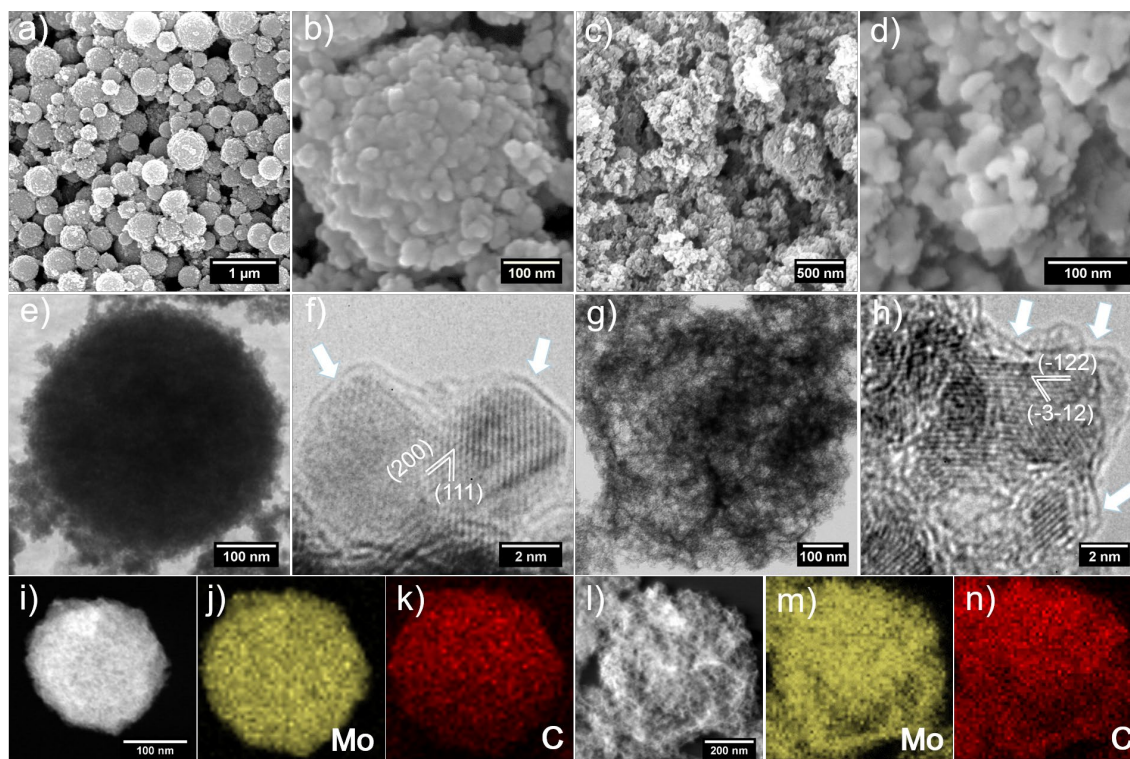


Figure 2. SEM images of (a,b) MoC/C and (c,d) MoC@C. (e) TEM and (f) HRTEM images of MoC/C. (g) TEM and (h) HRTEM images of MoC@C. Dark-field STEM images of (i) MoC/C and (l) MoC@C. EDS elemental mapping of (j) Mo and (k) C in MoC/C, and EDS elemental mapping of (m) Mo and (n) C in MoC@C.

High resolution TEM (HRTEM) images show the small diameter of the MoC particles in MoC/C (Figure 2f) and MoC@C (Figure 2h). Although the carbonization time is short (less than 15 s), the resultant MoC nanoparticles exhibit good crystallinity. A HRTEM image of MoC/C (Figure 2f) shows the well-crystallized MoC nanoparticles, for which the lattice fringes can be indexed to the (200) and (111) planes of cubic MoC. The MoC nanoparticles are coated with a relatively thin carbon layer, arrows in Figure 2f indicating that typically only one layer of carbon was found on the surface of the MoC nanoparticles. In contrast, MoC nanoparticles in MoC@C were usually covered by more than 3 layers of carbon, as indicated by arrows in Figure 2h; the nanoparticles shown in

Figure 2h show clear lattice fringes from the (-122) and (-3-12) planes of cubic MoC.

Dark field images from scanning TEM (STEM) showed solid particles in MoC/C (Figure 2i) and porous particles in MoC@C (Figure 2l). The corresponding energy dispersive X-ray spectroscopy (EDS) elemental mapping revealed that the MoC particles were homogeneously distributed both in the MoC/C (Figure 2j and Figure 2k) and in the MoC@C (Figure 2m and Figure 2n).

The overall structures of the samples were revealed by XRD experiments. Cubic phase MoC (JCPDS No. 65-280, $a = 4.273 \text{ \AA}$) exists in both the MoC/C and the MoC@C samples (Figure 3a). The peaks can be assigned to diffraction from the (111), (200), (220), and (311) planes. The broad peaks correlate with the small particle size of MoC, the sizes estimated from the Scherrer equation being 3.9 nm for MoC/C and 3.5 nm for MoC@C, in good accordance with those shown by TEM images. The broad peak near 25° is attributed to the (002) planes of graphitic carbon species.²⁰ No other phase can be detected besides MoC and C, suggesting that fast pyrolysis generates a high purity MoC phase. The presence of graphitic carbon in the MoC/C and the MoC@C was confirmed by Raman spectra (Figure 3b). The G band near 1580 cm^{-1} is associated with graphitic carbon and the D band near 1340 cm^{-1} corresponds to defective carbon.^{23, 27} The intensity ratio of D-band to G-band (i.e. I_D/I_G) is 0.97 for MoC/C and 0.93 for MoC@C. The value of I_D/I_G is comparable to that of graphene layers synthesized by long-time carbonization,^{26, 31} suggesting that the graphene formed in $\leq 15 \text{ s}$ will possess the good conductivity required for an efficient HER. The weight content of MoC was estimated by TGA (Section 3 and Figure S5, SI), being 86 wt% for the MoC/C and 61 wt% for the MoC@C. The weight content of molybdenum carbide in the MoC/C is higher than typical literature values (30-70 wt%),^{15, 19-20, 23, 25, 29} in accordance with an ultrathin carbon layer on the surface of the MoC particles in MoC/C. The BET surface area of MoC/C is $23.57 \text{ m}^2 \text{ g}^{-1}$, while that of MoC@C is $149.4 \text{ m}^2 \text{ g}^{-1}$ (Figure 3c).

XPS analyses were carried out to elucidate the electronic structures of MoC/C and

MoC@C. The XPS spectrum of MoC/C (Figure 3d) shows a strong peak corresponding to Mo³⁺ (228.8 eV) and a small peak corresponding to Mo²⁺ (228.5 eV) which are associated with MoC;²⁵⁻²⁶ weak peaks arising from Mo⁴⁺ (229.8 eV) and Mo⁵⁺ (232.3 eV) were also found, resulting from the molybdenum oxide arising from air exposure.²⁰ The C 1s spectrum of MoC/C (Figure 3e) contains three peaks at 283.8, 284.8 and 286.0 eV, which are assigned to C-Mo, C-C/C=C and C=O, respectively.^{22, 28} The Mo and C XPS spectra of MoC@C are nearly identical to those of MoC/C. The shifts of the binding energies for Mo and C in MoC are ca. 0.1 eV. The intensity of the C-C/C=C peak in MoC/C is weaker than that in MoC@C, in accordance with a larger MoC content in MoC/C.

The valence band XPS spectra (Figure 3f) show that, in comparison with MoC@C, the density of states and thereby the d-band center of MoC/C is displaced towards the Fermi level. According to d-band theory,⁴⁶ the interaction between hydrogen and MoC/C is stronger than that between hydrogen and MoC@C, making the MoC/C a better candidate electrocatalyst for the HER.^{17, 27}

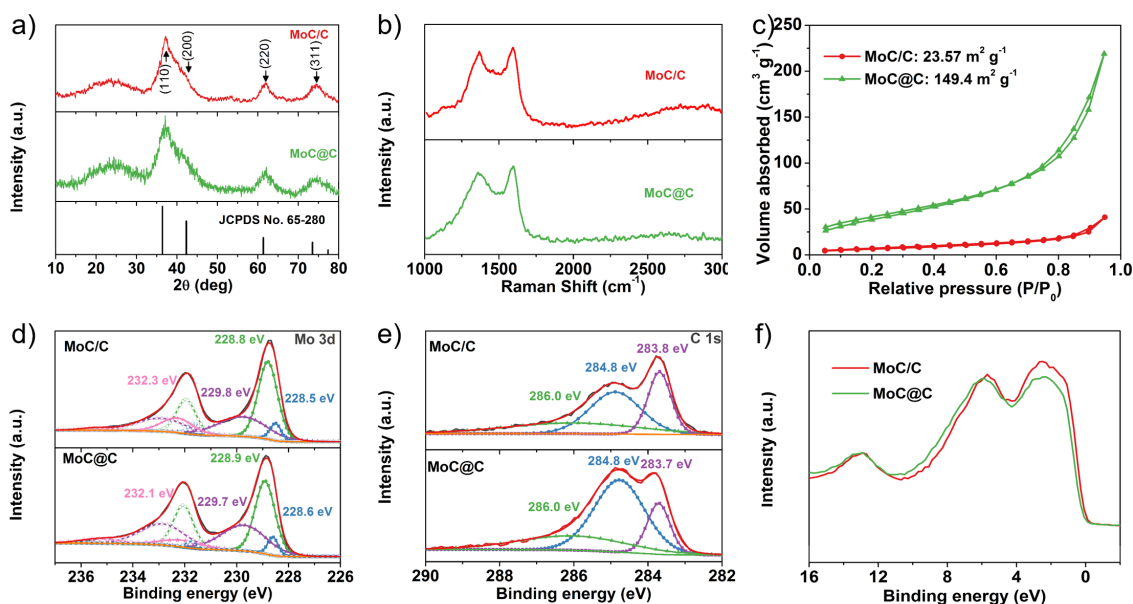


Figure 3. (a) XRD patterns, (b) Raman spectra, and (c) Nitrogen adsorption-desorption isotherms of MoC/C and MoC@C. (d) Mo 3d windows and (e) C 1s windows of the XPS spectra of MoC/C and MoC@C. (f) Valence band XPS spectra of MoC/C and MoC@C.

Figure 4a displays polarization curves of MoC/C, MoC@C, a benchmark Pt/C catalyst (20 wt% Pt on carbon black from Johnson Matthey), and a bare glassy carbon electrode (GCE) in 0.5 M H₂SO₄. MoC/C and MoC@C show large current densities when the potential is more negative than -0.1 V vs. reversible hydrogen evolution (RHE) potential, whereas the GCE shows negligible current. The overpotential required to drive a current density of 20 mA cm⁻² (η_{20}) is widely employed as an indicator of HER performance, because solar cells typically produce a current density of 10-20 mA cm⁻² under AM 1.5G illumination.⁴⁷ The η_{20} is 144 mV for MoC/C and 157 mV for MoC@C in acidic solution. The influence of growth temperature on the HER performance was explored (Figure S6), confirming that the performance shown in Figure 4a is the best performance for MoC/C and MoC@C. MoC/C and MoC@C are also efficient electrocatalysts in basic solution (Figure S7a), with η_{20} values of 220 mV and 250 mV, respectively. The polarization curves result in Tafel slopes of 63.6 mV dec⁻¹ for MoC/C and 93.3 mV dec⁻¹ for MoC@C in acidic solution (Figure 4b). In basic solution, the Tafel slopes are 89.0 mV dec⁻¹ for MoC/C and 114 mV dec⁻¹ for MoC@C (Figure S7b). The Tafel slope lies between 40 and 120 mV dec⁻¹ for both MoC/C and MoC@C, and therefore the HER process should proceed by a Volmer-Heyrovsky mechanism, which consists of a discharge of a proton (Volmer reaction: H₃O⁺ + e⁻ → H_{ads} + H₂O) followed by electrochemical recombination with an additional proton (Heyrovsky reaction: H_{ads} + H₃O⁺ + e⁻ → H₂ + H₂O).¹⁵ The Tafel slope of MoC@C is closer to the characteristic value of the Volmer reaction (120 mV dec⁻¹) than the corresponding Tafel slope of MoC/C, suggesting that the HER on the surface of MoC@C is more limited by the absorption of protons, i.e. the absorption of protons on the surface of MoC@C is less

efficient than proton absorption on MoC/C.

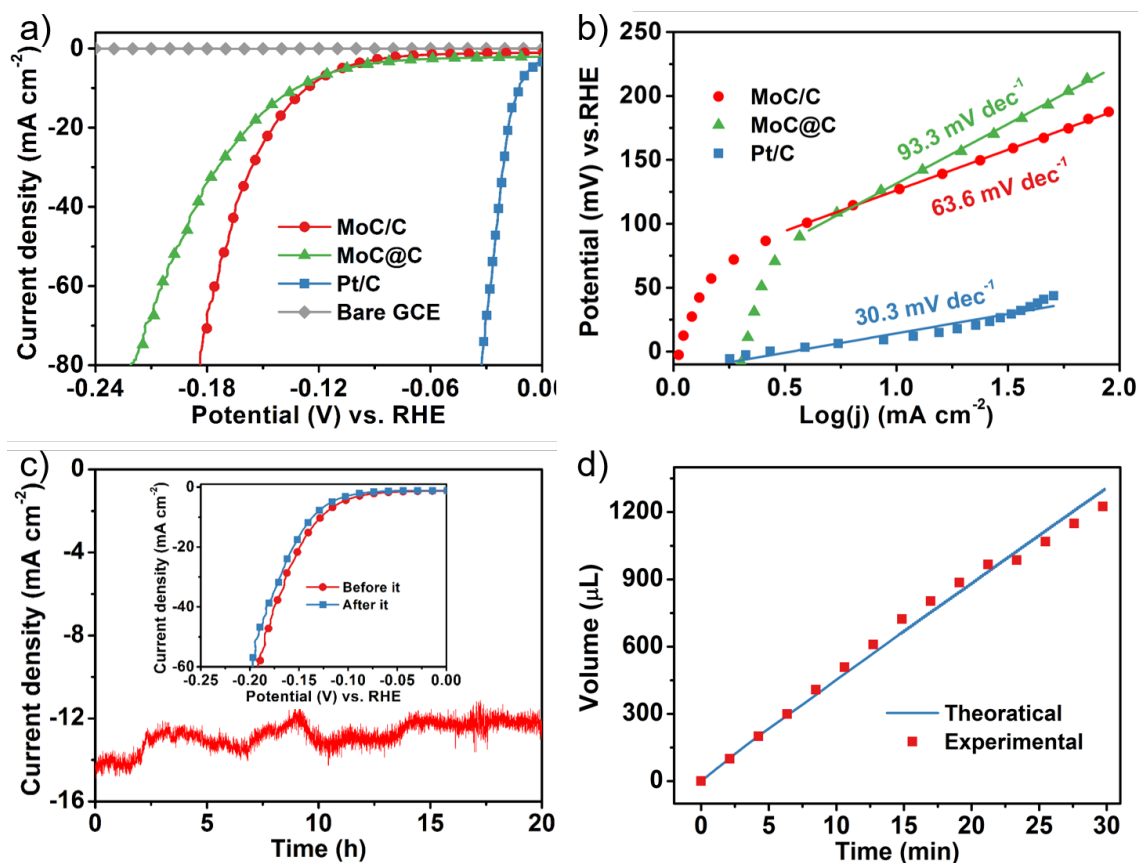


Figure 4. (a) Polarization curves and (b) corresponding Tafel plots of MoC/C, MoC@C, Pt/C and bare GCE. Potentials in (a) and (b) were corrected for the iR drop. (c) Amperometric (*i-t*) curve of MoC/C. Inset of (c) shows polarization curves measured before and after *i-t* measurement. (d) Comparison of theoretical and experimental volumes of hydrogen generated in a potentiostatic electrolysis. All measurements were carried out in 0.5 M H_2SO_4 .

The performance of MoC/C is superior to that of MoC@C in both acidic and basic solutions, although the BET surface area of MoC@C is ca. 6 times that of MoC/C. It has been claimed that the performance measured with Pt as the counter electrode may be overestimated because Pt leached from the counter electrode might be re-deposited on the

working electrode.²⁹⁻³⁰ The performance of MoC/C was therefore measured with a graphite rod as a counter electrode in our experiments, with MoC/C exhibiting a η_{20} value as low as 144 mV in acidic solution, which is superior to most carbides measured under the same experimental set-up^{14-15, 19, 23-25, 27, 29, 48-50} (see Table S1). MoC/C is one of the most efficient carbide electrocatalysts, although MoC is not even the most active phase of molybdenum carbide (β -Mo₂C).¹⁷ In particular, MoC/C is superior to carbides whose performance has been enhanced by various strategies, including the increase of surface area by the formation of mesoporous Mo₂C nano-octahedrons (η_{20} = 160 mV)²³ or Mo₂C dispersed on a hierarchical carbon micro-flower (η_{10} = 144 mV),³⁰ the composition modulation by the construction of Mo₂C-MoC composite nanowires (η_{20} = 152 mV)²⁷ or Mo₂C-WC composite nanowires (η_{20} = 150 mV),²⁴ the doping of Mo₂C by Fe (η_{10} = 300 mV)⁵¹ or Co (η_{10} = 140 mV),⁵² as well as the doping of graphene support by nitrogen (η_{10} = 124 mV).¹⁹ It is worth noting that our strategy, reducing surface carbon coating, is compatible to procedures controlling the phase, size, doping of carbides and doping of carbon supports. The integration of our strategy to the aforementioned ones may result in a further improvement in performance of carbides, advancing the promising applications of carbides in the HER.

MoC/C effects sustained electrolysis in both acidic and basic media, which is a prerequisite for potential large-scale applications. In acidic solution, the catalytic current density remained at ca. 12 mA cm⁻² at -0.135 mV vs. RHE over 20 h of potentiostatic electrolysis (Figure 4c), while the value of η_{20} was increased by only 9 mV after 20 h pyrolysis (inset of Figure 4c). In basic solution, the current density maintained 86% of its initial value after potentiostatic electrolysis for 20 h, the variation in η_{20} being just 14 mV (Figure S7c). Faradaic efficiencies of 95% in acidic solution (Figure 4d) and 94% in basic solution (Figure S7d) were derived from comparison of the theoretical and experimental volumes of generated hydrogen during potentiostatic electrolysis, confirming that the large currents shown in Figure 4a are associated with reduction of H⁺ to H₂.

The kinetic aspects of the surface HER were investigated by electrochemical impedance spectroscopy (EIS) (Figure 5a). The reaction kinetics of the HER occurring on the surface of the electrocatalyst usually correlate with charge-transfer resistance (R_{ct}), a smaller R_{ct} suggesting a faster surface reaction rate. Data fitting of the EIS spectra using an equivalent circuit (Figure S8 and Table S2) resulted in R_{ct} values of 62.48 Ω for MoC/C and 101.9 Ω for MoC@C. The smaller R_{ct} value for MoC/C is consistent with faster reaction kinetics on the surface of MoC/C in comparison with MoC@C.

The reaction rate of the HER on the surface of an electrocatalyst is determined both by the number of active sites and the intrinsic catalytic activity of each active site. The number of active sites is correlated with the electrochemically active surface area (EASA).⁵³ The EASAs of the two samples were derived from the specific capacitances measured using CV scans (Section 4 and Figure S9, SI). The specific capacitances are 16.5 mF cm⁻² for MoC/C and 26.2 mF cm⁻² for MoC@C (Figure 5b), affording EASA values of 413 cm² for MoC/C and 655 cm² for MoC@C; the EASA of MoC@C is therefore ca. 1.6 times that of MoC/C. The number of active sites in MoC/C is therefore much less than that in MoC@C, and the superior performance of MoC/C cannot be attributed to its surface area.

The intrinsic performances of the samples J_{EASA} were evaluated from the current densities computed by normalizing the polarization currents with the EASA values, but not by the project area. Figure 5c shows clearly that MoC/C affords a J_{EASA} value larger than that of MoC@C; at an overpotential of 150 mV, the J_{EASA} is 4.2 $\mu\text{A cm}^{-2}$ for MoC/C and 1.8 $\mu\text{A cm}^{-2}$ for MoC@C. The J_{EASA} data are consistent with the intrinsic catalytic activity of MoC/C being far superior to that of MoC@C.

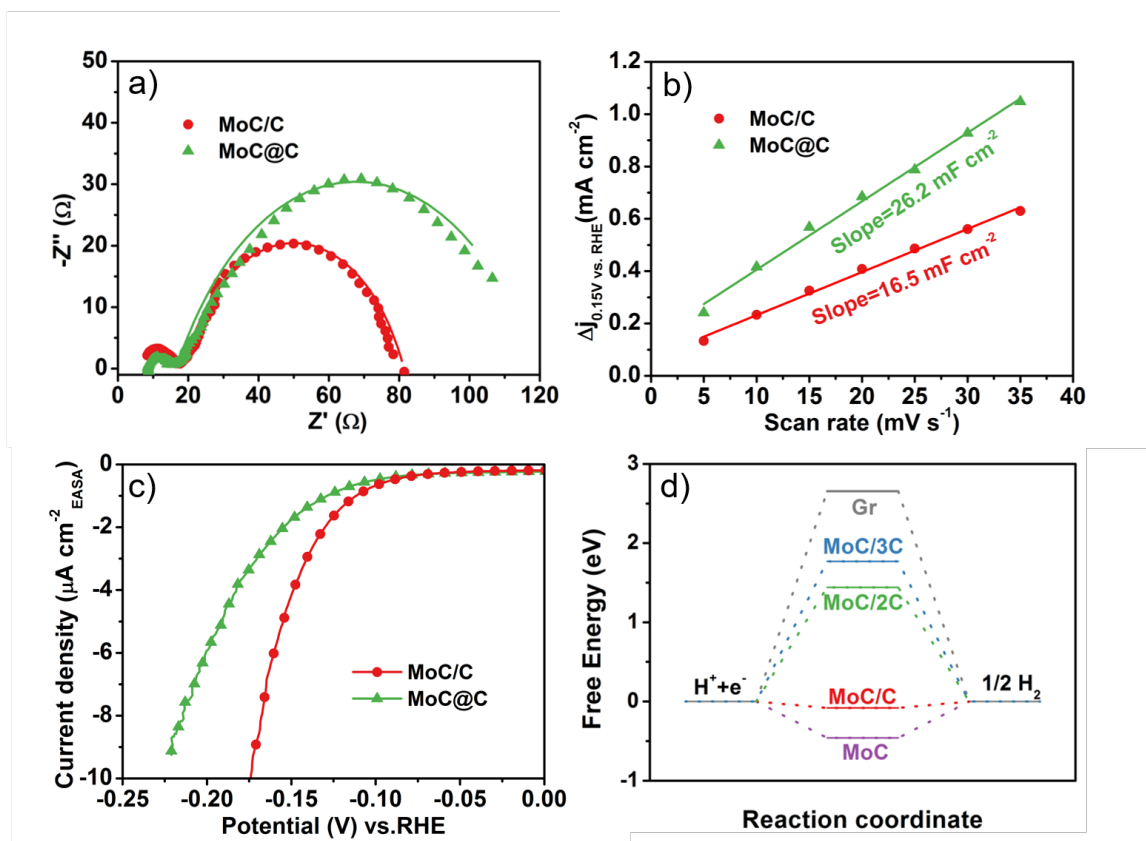


Figure 5. (a) EIS spectra of MoC/C and MoC@C measured at -0.2 V vs RHE. (b) Capacitive current of MoC/C and MoC@C at 0.15 V vs RHE as a function of scan rate. (c) Reductive current of MoC/C and MoC@C normalized by the EASA. (d) Free energy diagram for the HER of the calculated systems.

The structural and morphological features of MoC/C and MoC@C are summarized in Table 1. MoC/C and MoC@C have the same crystal structure, but MoC/C has a larger particle size and a much smaller surface area than MoC@C, so the difference in intrinsic activity of MoC/C and MoC@C should be ascribed to the difference in the thickness of the carbon layer coatings on the surface of the MoC nanoparticles, with the thinner carbon coating corresponding to better performance.

Table 1. Summary of structural and morphological features and performance.

Sample	Structure ^[a]	Particle size ^[b] (nm)	BET area (m ² /g)	Carbon layer ^[c]	J _{EASA-150} ^[d] (μ A/cm ²)
MoC/C	Cubic	3.9	23.57	1	4.2
MoC@C	Cubic	3.5	149.4	≥ 3	1.8

[a] Both indexed to JCPDS No. 65-280. [b] Sizes estimated from XRD patterns. [c] Number of carbon layers on the surface of the MoC particles, obtained from the HRTEM images. [d] Current normalized by the EASA at -150 mV vs RHE.

DFT calculations were carried out to understand the influence of the thickness of surface carbon coating on the catalytic activity in the HER (see Section 5 and Figure S10, SI). The free energy of hydrogen adsorption (ΔG_H) was adopted as a reasonable descriptor of hydrogen evolution activity. The ΔG_H of a good hydrogen evolution electrocatalyst should be ~ 0 eV.² The results of the computational studies are shown in Figure 5d. According to the DFT calculations, the ΔG_H of single layer graphene is 2.655 eV. This large endothermic ΔG_H suggests that the interaction of hydrogen and graphene is energetically unfavorable. The (111) surface of MoC has a ΔG_H of -0.459 eV, implying that bare MoC is active in the HER. The ΔG_H becomes -0.081 eV when the (111) surface of MoC is covered with one carbon layer (MoC/C), suggesting that the synergistic effect between MoC and an ultrathin surface carbon coating promotes the HER. An endothermic ΔG_H of 1.442 eV is obtained for the (111) MoC surface covered with two layers of graphene (MoC/2C) while a ΔG_H of 1.770 eV is obtained for the (111) MoC surface covered with three layers of carbon (MoC/3C), indicating that a coating of multiple layers of carbon will suppress the catalytic activity of MoC/2C and MoC/3C. The synergistic effect comes from the different absorption proclivities of hydrogen on MoC and graphene surface, i.e. hydrogen can be bound on the MoC surface whereas the

absorption of hydrogen on a graphene surface is relatively unfavorable. The covering of the MoC surface with a graphene layer would mitigate the binding strength of hydrogen on the surface. With a one-carbon-layer coating, the ΔG_{H} of MoC/C moves from -0.459 eV of MoC in the positive direction to -0.081 eV, which is more favorable for the HER than that of the bare MoC surface. This mechanism of absorption free energy modulation is analogous to that which has been utilized to produce a HER active electrocatalyst (Cu-Ti) from two poor hydrogen evolution catalysts (Cu and Ti).⁵⁴ When the thickness of the graphene layer is increased, the composite system loses the characteristics of MoC and behaves more like a graphene surface, resulting in a more positive ΔG_{H} that reduces the HER activity. From this perspective, the interaction between the MoC-graphene composite and hydrogen decreases with increasing number of graphene layers. The stronger H* adsorption at MoC/C than at MoC@C is consistent with the results from the valence band XPS spectra (Figure 3f), which show that the d-band center of MoC/C is closer to the Fermi level than that of MoC@C, and consistent with the Tafel slopes (Figure 4b), which suggest more efficient absorption of protons by MoC/C. The DFT calculations show that the performance of MoC is sensitive to the surface carbon coating, with a thick carbon coating severely diminishing the HER activity.

CONCLUSION

In conclusion, the significant influence of the thickness of surface carbon coating on the HER performance of molybdenum carbide has been demonstrated, and a facile and scalable approach has been developed for the synthesis of MoC coated with a relatively thin carbon layer that can efficiently catalyze the HER and that possesses excellent long-term stability. The η_{20} value is low (144 mV in acidic solution), ranking MoC/C amongst the best molybdenum carbide electrocatalysts. The HER catalytic activity of MoC/C is superior to that of MoC@C, although the surface area of MoC/C is only 16% of that of MoC@C. The performance difference originates from the thickness of the

carbon layer coating the MoC nanoparticles. The influence of the thickness of the carbon layer on the HER performance was confirmed by the DFT calculations.

Supporting Information.

XRD patterns, XPS spectra, SEM and TEM images, TGA curves, LSV and CV curves, and models for DFT calculations. This material is available free of charge via the Internet at <http://pubs.acs.org>.

ACKNOWLEDGMENT

This research was financially supported by the National Natural Science Foundation of China (61006049, 51172100, 51432006). M.G.H. thanks the Australian Research Council for support.

REFERENCES

1. Turner, J. A., *Science* **2004**, *305*, 972-974.
2. Hinnemann, B.; Moses, P. G.; Bonde, J.; Jørgensen, K. P.; Nielsen, J. H.; Horch, S.; Chorkendorff, I.; Nørskov, J. K., *J. Am. Chem. Soc.* **2005**, *127*, 5308-5309.
3. Jaramillo, T. F.; Jørgensen, K. P.; Bonde, J.; Nielsen, J. H.; Horch, S.; Chorkendorff, I., *Science* **2007**, *317*, 100-102.
4. Li, Y. G.; Wang, H. L.; Xie, L. M.; Liang, Y. Y.; Hong, G. S.; Dai, H. J., *J. Am. Chem. Soc.* **2011**, *133*, 7296-7299.
5. Merki, D.; Fierro, S.; Vrubel, H.; Hu, X. L., *Chem. Sci.* **2011**, *2*, 1262-1267.
6. Popczun, E. J.; McKone, J. R.; Read, C. G.; Biacchi, A. J.; Wiltrout, A. M.; Lewis, N. S.; Schaak, R. E., *J. Am. Chem. Soc.* **2013**, *135*, 9267-9270.

7. Liu, Q.; Tian, J. Q.; Cui, W.; Jiang, P.; Cheng, N. Y.; Asiri, A. M.; Sun, X. P., *Angew. Chem. Int. Ed.* **2014**, *53*, 6710-6714.
8. Huang, Z. P.; Chen, Z. B.; Chen, Z. Z.; Lv, C. C.; Meng, H.; Zhang, C., *ACS Nano* **2014**, *8*, 8121-8129.
9. Huang, Z. P.; Chen, Z. Z.; Chen, Z. B.; Lv, C. C.; Humphrey, M. G.; Zhang, C., *Nano Energy* **2014**, *9*, 373-382.
10. Wang, X. G.; Kolen'ko, V. V.; Bao, X. Q.; Kovnir, K.; Liu, L. F., *Angew. Chem. Int. Ed.* **2015**, *54*, 8188-8192
11. Vrubel, H.; Hu, X., *Angew. Chem. Int. Ed.* **2012**, *51*, 12703-12706.
12. Zheng, Y.; Jiao, Y.; Zhu, Y. H.; Li, L. H.; Han, Y.; Chen, Y.; Du, A. J.; Jaroniec, M.; Qiao, S. Z., *Nat. Commun.* **2014**, *5*.
13. Zheng, Y.; Jiao, Y.; Li, L. H.; Xing, T.; Chen, Y.; Jaroniec, M.; Qiao, S. Z., *ACS Nano* **2014**, *8*, 5290-5296.
14. Chen, W. F.; Wang, C. H.; Sasaki, K.; Marinkovic, N.; Xu, W.; Muckerman, J. T.; Zhub, Y.; Adzic, R. R., *Energy Environ. Sci.* **2013**, *6*, 943-951.
15. Chen, W.; Iyer, S.; Iyer, S.; Sasaki, K.; Wang, C.; Zhu, Y.; Muckerman, T. J.; Fujita, E., *Energy Environ. Sci.* **2013**, *6*, 1818-1826.
16. Liao, L.; Wang, S.; Xiao, J.; Bian, X.; Zhang, Y.; Scanlon, M. D.; Hu, X.; Tang, Y.; Liu, B.; Girault, H. H., *Energy Environ. Sci.* **2014**, *7*, 387-392.
17. Wan, C.; Regmi, Y. N.; Leonard, B. M., *Angew. Chem. Int. Ed.* **2014**, *126*, 6525-6528.
18. Cheng, W.; Leonard, B. M., *Chem. Mater.* **2015**, *27*, 4281-4288.
19. Liu, Y.; Yu, G.; Li, G.; Sun, Y.; Asefa, T.; Chen, W.; Zou, X., *Angew. Chem. Int. Ed.* **2015**, *54*, 10752-10757.
20. Ma, R.; Zhou, Y.; Chen, Y.; Li, P.; Liu, Q.; Wang, J., *Angew. Chem. Int. Ed.* **2015**, *54*, 14723-14727.

21. Ma, F.; Wu, H.; Xia, B.; Xu, C.; Lou, X., *Angew. Chem. Int. Ed.* **2015**, *54*, 15395-15399.
22. Tang, Y. J.; Gao, M. R.; Liu, C. H.; Li, S. L.; Jiang, H. L.; Lan, Y. Q.; Han, M.; Yu, S. H., *Angew. Chem. Int. Ed.* **2015**, *54*, 12928-12932.
23. Wu, H.; Xia, B.; Yu, L.; Yu, X.; Lou, X., *Nat. Commun.* **2015**, *6*, 6512-6519.
24. Xiao, P.; Ge, X.; Wang, H.; Liu, Z.; Fisher, A.; Wang, X., *Adv. Funct. Mater.* **2015**, *25*, 1520-1526.
25. Ang, H.; Wang, H.; Li, B.; Zong, Y.; Wang, X.; Yan, Q., *Small* **2016**, *12*, 2859-2865.
26. Li, J.; Wang, Y.; Liu, C.; Li, S.; Wang, Y.; Dong, L.; Dai, Z.; Li, Y.; Lan, Y., *Nat. Commun.* **2016**, *7*, 11204-11211.
27. Lin, H.; Shi, Z.; He, S.; Yu, X.; Wang, S.; Gao, Q.; Tang, Y., *Chem. Sci.* **2016**, *7*, 3399-3405.
28. Wang, J.; Xia, H.; Peng, Z.; Lv, C.; Jin, L.; Zhao, Y.; Huang, Z.; Zhang, C., *ChemSusChem* **2016**, *9*, 855-862.
29. Gong, Q. F.; Wang, Y.; Hu, Q.; Zhou, J. G.; Feng, R. F.; Duchesne, P. N.; Zhang, P.; Chen, F. G.; Han, N.; Li, Y. F.; Jin, C. H.; Li, Y. G.; Lee, S. T., *Nat. Commun.* **2016**, *7*, 13216-13222.
30. Huang, Y.; Gong, Q. F.; Song, X. L.; Feng, K.; Nie, K. Q.; Zhao, F. P.; Wang, Y. Y.; Zeng, M.; Zhong, J.; Li, Y. G., *ACS Nano* **2016**, 10.1021/acsnano.6b06580.
31. Wu, Z. Y.; Hu, B. C.; Wu, P.; Liang, H. W.; Yu, Z. L.; Lin, Y.; Zheng, Y. R.; Li, Z. Y.; Yu, S. H., *NPG Asia Mater.* **2016**, *8*, e288.
32. Ang, H. X.; Tian, H. T.; Luo, Z. M.; Zhang, Y.; Guo, Y. Y.; Guo, G. L.; Zhang, H.; Yan, Q. Y., *Small* **2015**, *11*, 6278-6284
33. Kimmel, Y. C.; Esposito, D. V.; Birkmire, R. W.; Chen, J. G. G., *Inter. J. Hydrogen Energy* **2012**, *37*, 3019-3024.
34. Hunt, S. T.; Nimmanwudipong, T.; Roman-Leshkov, Y., *Angew. Chem. Int. Ed.* **2014**, *53*, 5131-5136.

35. Yang, X. F.; Kimmel, Y. C.; Fu, J.; Koel, B. E.; Chen, J. G. G., *ACS Catal.* **2012**, *2*, 765-769.
36. Kwak, W. J.; Lau, K. C.; Shin, C. D.; Amine, K.; Curtiss, L. A.; Sun, Y. K., *ACS Nano* **2015**, *9*, 4129-4137.
37. Yan, Z. X.; He, G. Q.; Shen, P. K.; Luo, Z. B.; Xie, J. M.; Chen, M., *J. Mater. Chem. A* **2014**, *2*, 4014-4022.
38. Wu, M. X.; Lin, X. A.; Hagfeldt, A.; Ma, T. L., *Angew. Chem. Int. Ed.* **2011**, *50*, 3520-3524
39. Wu, M. X.; Lin, X.; Wang, Y. D.; Wang, L.; Guo, W.; Qu, D. D.; Peng, X. J.; Hagfeldt, A.; Gratzel, M.; Ma, T. L., *J. Am. Chem. Soc.* **2012**, *134*, 3419-3428.
40. Motl, N. E.; Mann, A. K. P.; Skrabalak, S. E., *Journal of Materials Chemistry A* **2013**, *1*, 5193-5202.
41. Limberg, C.; Boese, R.; Schiemenz, B., *J. Chem. Soc., Dalton Trans.* **1997**, 1633-1637.
42. Alhajri, N. S.; Anjum, D. H.; Takanahe, K., *J. Mater. Chem. A* **2014**, *2*, 10548-10556.
43. Lv, C. C.; Wang, J.; Huang, Q. L.; Yang, Q. P.; Huang, Z. P.; Zhang, C., *Rsc Advances* **2016**, *6*, 75870-75874.
44. Rummeli, M. H.; Kramberger, C.; Gruneis, A.; Ayala, P.; Gemming, T.; Buchner, B.; Pichler, T., *Chem. Mater.* **2007**, *19*, 4105-4107.
45. Liu, B. L.; Tang, D. M.; Sun, C. H.; Liu, C.; Ren, W. C.; Li, F.; Yu, W. J.; Yin, L. C.; Zhang, L. L.; Jiang, C. B.; Cheng, H. M., *J. Am. Chem. Soc.* **2011**, *133*, 197-199.
46. Hammer, B.; Norskov, J. K., *Nature* **1995**, *376*, 238-240.
47. Walter, M. G.; Warren, E. L.; McKone, J. R.; Boettcher, S. W.; Mi, Q. X.; Santori, E. A.; Lewis, N. S., *Chem. Rev.* **2010**, *110*, 6446-6473.
48. Shi, Z.; Wang, Y.; Lin, H.; Zhang, H.; Shen, M.; Xie, S.; Zhang, Y.; Gao, Q.; Tang, Y., *J. Mater. Chem. A* **2016**, *4*, 6006-6013.

49. Ma, L.; Ting, L. R. L.; Molinari, V.; Giordano, G.; Yeo, B. S., *J. Mater. Chem. A* **2015**, *3*, 8361-8368.
50. He, C. Y.; Tao, J. Z., *Chem. Commun.* **2015**, *51*, 8323-8325.
51. Wan, C.; Leonard, B. M., *Chem. Mater.* **2015**, *27*, 4281-4288.
52. Lin, H. L.; Liu, N.; Shi, Z. P.; Guo, Y. L.; Tang, Y.; Gao, Q. S., *Adv. Funct. Mater.* **2016**, *26*, 5590-5598.
53. Benck, J. D.; Hellstern, T. R.; Kibsgaard, J.; Chakthranont, P.; Jaramillo, T. F., *ACS Catal.* **2014**, *4*, 3957-3971.
54. Lu, Q.; Hutchings, G. S.; Yu, W. T.; Zhou, Y.; Forest, R. V.; Tao, R. Z.; Rosen, J.; Yonemoto, B. T.; Cao, Z. Y.; Zheng, H. M.; Xiao, J. Q.; Jiao, F.; Chen, J. G. G., *Nature Commun.* **2015**, *6*, 6567.

TOC Graphic

